Eur Radiol (2015) 25:2049–2058
DOI 10.1007/s00330-014-3577-z

MAGNETIC RESONANCE

Whole-body intravoxel incoherent motion imaging

Lukas Filli · Moritz C. Wurnig · Roger Luechinger · Christian Eberhardt · Roman Guggenberger · Andreas Boss

Received: 28 July 2014 / Revised: 7 December 2014 / Accepted: 18 December 2014 / Published online: 10 January 2015

Abstract
Objectives To investigate the technical feasibility of whole-body intravoxel incoherent motion (IVIM) imaging.
Materials and Methods Whole-body MR images of eight healthy volunteers were acquired at 3T using a spin-echo echo-planar imaging sequence with eight b-values. Coronal parametrical whole-body maps of diffusion (D), pseudodiffusion (D*), and the perfusion fraction (F_p) were calculated. Image quality was rated qualitatively by two independent radiologists, and inter-reader reliability was tested with intra-class correlation coefficients (ICCs). Region of interest (ROI) analysis was performed in the brain, liver, kidney, and erector spinae muscle.
Results Depiction of anatomic structures was rated as good on D maps and good to fair on D* and F_p maps. Exemplary mean D (10^{-3} mm^2/s), D* (10^{-3} mm^2/s) and F_p (%) values (± standard deviation) of the renal cortex were as follows: 1.7± 0.2; 15.6±6.5; 20.9±4.4. Inter-observer agreement was "substantial" to "almost perfect" (ICC=0.80 – 0.92). The coefficient of variation of D* was significantly lower with the proposed algorithm compared to the conventional algorithm ($p<0.001$), indicating higher stability.
Conclusion The proposed IVIM protocol allows computation of parametrical maps with good to fair image quality. Potential future clinical applications may include characterization of widespread disease such as metastatic tumours or inflammatory myopathies.

L. Filli (✉) · M. C. Wurnig · C. Eberhardt · R. Guggenberger · A. Boss
Department of Radiology, University Hospital Zurich, Ramistrasse 100, 8091 Zurich, Switzerland
e-mail: lukas.filli@usz.ch

R. Luechinger
Institute of Biomedical Technology, University and ETH Zurich, Zurich, Switzerland

Key Points
- *IVIM imaging allows estimation of tissue perfusion based on diffusion-weighted MRI.*
- *In this study, a clinically suitable whole-body IVIM algorithm is presented.*
- *Coronal parametrical whole-body maps showed good depiction of anatomic details.*
- *Potential future applications include detection of widespread metastatic or inflammatory disease.*

Keywords Whole body · Intravoxel incoherent motion · Diffusion-weighted imaging · Magnetic resonance · Pseudodiffusion

Introduction

Diffusion-weighted magnetic resonance imaging (DWI) is widely used for disease detection and characterization of focal lesions, particularly tumours, in different organs [1]. Many tumours exhibit a diffusion restriction compared to surrounding healthy parenchyma due to their high cellularity. The degree of diffusion restriction of water molecules in tissue is quantified with the apparent diffusion coefficient (ADC) in units of mm^2/s. The determination of the ADC is based on the assumption of a mono-exponential relationship between b-value and signal intensity given by the equation

$$Sb/S0 = \exp(-b \times ADC) \quad (1)$$

where S_b is the signal intensity depending on the b-value, and S_0 is the signal intensity when the b-value is zero. The b-value is a sequence parameter that adjusts the degree of diffusion weighting of the DWI sequence by different strength and duration of the diffusion gradients.

However, for low b-values, typically below 150 s/mm^2, the measured signal not only reflects pure molecular water diffusion, but also "pseudodiffusion" resulting from fast moving water molecules, e.g. in the capillaries [2–7]. Based on the concept of intravoxel incoherent motion (IVIM), the contribution of both diffusion and pseudodiffusion to the signal intensity is described by a bi-exponential relationship between b-value and signal intensity according to the following equation:

$$Sb/S0 = \left(1-F_p\right) \times \exp(-b \times D) + F_p \times \exp(-b \times D^*) \quad (2)$$

where D reflects pure molecular diffusion, D* is the pseudodiffusion, and F_p is the relative perfusion fraction.

Dedicated IVIM protocols have been applied for tissue characterization in a variety of organs, including the brain [8], liver [6, 9–12], kidneys [11, 13–15], and muscles [7, 11, 16, 17]. This is the first study to present a clinically suitable whole-body IVIM algorithm. By providing more comprehensive tissue characterization, whole-body IVIM may be advantageous over conventional whole-body DWI in the assessment of metastatic disease with hypervascular tumours, such as neuroendocrine tumours, renal cell carcinoma, or melanoma.

Materials and methods

Subjects

This prospective study was performed on eight healthy volunteers (four men, four women; mean age, 30.6 years; range, 24 – 35 years; mean body height, 1.74 m; range, 1.65 – 1.86 m). Approval by the local ethics committee was obtained. All individuals gave written informed consent to the MR examination and subsequent scientific evaluation of the data sets. Three subjects (two men, one woman; age range, 24 – 31 years) underwent a second scan 4 months after the initial visit in order to assess the repeatability of D, D*, and F_p.

Imaging protocol

All scans were performed on a 3 Tesla whole-body MR scanner (Ingenia, Philips Healthcare, Best, the Netherlands) using a 15-channel head coil, a 32-channel flexible anterior coil, and the integrated posterior coil. Images were acquired using a spin-echo prepared echo-planar imaging (EPI) sequence in transversal orientation during free breathing. The MR protocol consisted of three (head to proximal femur) to six (whole body) stacks of axial slices, each with a field of view of 450 (right to left) x 295 (anterior to posterior) x 300 (head to feet) mm^3. Imaging parameters were as follows: TR, 8,708 ms; TI, 220 ms; TE, 64 ms; voxel size, 3.5×3.5×6 mm^3; EPI factor, 29; SENSE factor, 3; acquisition matrix, 128×81; number of signal averages, 3; b-values, 0, 10, 20, 50, 150, 300, 500, and 800 s/mm^2. Fat suppression was performed using spectral selection attenuated inversion recovery (SPAIR). The baseline scanning position was set at the jugular notch, with one image stack above and the other ones below this reference level.

Post-processing

The initial images were processed for the IVIM analysis using Matlab (The MathWorks, Natick, MA, USA) implemented by A.B.. with more than 10 years of experience in MRI post-processing. Parametric maps of D, D*, and F_p were calculated on a pixel-wise basis using Matlab routines. Initial stacks of axial image data sets were linked together and reformatted in the coronal orientation. Noise was measured as the standard deviation in a region of interest (ROI) placed in the background, and noise-correction was performed on the data sets by squared subtraction according to Gudbjartsson [18].

To obtain D, D*, and F_p values, a multi-step IVIM approach was applied on the bi-exponential relationship describing the measured signal decay:

a) Because of the absence of perfusion effects at higher b-values, the term reflecting pseudodiffusion in Eq. (2) can be disregarded and the signal decay is described by a mono-exponential relation. D was computed by a linear least-squares fit to the log-transformed signal intensities for b-values≥150 s/mm^2. D corresponds to the slope and S_0' with $S_0'=S_0\ (1 - F_p)$ to the y-axis intercept of the regression line:

$$\log S_b = -D \cdot b + \log S_0' \quad (3)$$

b) The perfusion fraction F_p was then calculated from the measured signal intensity of the b0-measurement S_0 and the calculated S_0':

$$F_p = \frac{S_0 - S_0'}{S_0} \quad (4)$$

c) If F_p is≤0 or≥1, no pseudodiffusion is detectable and a mono-exponential fit to Eq. (1) is carried out with all b-values applying an algorithm based on the Levenberg-Marquardt algorithm recalculating D with higher precision. D* and F_p are both set to zero.

d) If $0<F_p<1$, a linear least-squares fit to the log-transformed signal intensities of the first 4 b-values was calculated with the slope denoting D*', which contains contributions from both diffusion and pseudodiffusion.

e) From D*', the pseudodiffusion coefficient D* was calculated based on the following equation:

$$D^* = \frac{D^{*\prime} - D}{F_p} + D \quad (5)$$

This algorithm is an approximation assuming nearly monoexponential signal decay for low b-values with an effective diffusion coefficient D*'. Equation (5) can be obtained using another approximation step for low b-values with a first-order Taylor series expansion of the exponentials in Eq. (2) replacing exp(x) with (1-x). This algorithm was presumed to provide more stable IVIM results compared to the conventional bilinear fitting algorithm [2]; this hypothesis was tested as described below.

Qualitative rating

Coronal and axial parametrical maps of D, D*, and F_p were rated qualitatively by two independent radiologists with 6 and 2 years of experience in MR imaging, respectively. A 4-point scale was used to rate the depiction of the brain, aorta, liver, renal cortex, and medulla on the different parametrical maps: 1 (excellent depiction), 2 (good depiction), 3 (fair depiction), 4 (poor depiction). Furthermore, the overall impression of image noise on D, D*, and F_p maps was defined based on another 4-point scale: 1 (very little noise), 2 (little noise), 3 (moderate noise), 4 (severe noise).

Measurement of IVIM parameters and quantitative analysis

IVIM parameters were measured by reader one in standardized ROIs on axial images in the cerebrospinal fluid (CSF, measured in the lateral ventricles; ROI size, 40±3 mm^2), cerebral gray matter (GM, measured in the striatum; 98±9 mm^2) and white matter (WM, measured in the corona radiata; 151±13 mm^2), liver (1398±218 mm^2), renal cortex (232±41 mm^2), renal medulla (81±6 mm^2), and erector spinae muscle (at the level of the kidneys; 431±10 mm^2). Large vascular structures such as the hepatic veins were avoided. Descriptive statistics were applied to the ROI analyses with the calculation of mean values and standard deviations.

In order to quantify the 'noise' on the parametrical maps, the coefficient of variation of D* and F_P (i.e., the standard deviation divided by the mean) was calculated in the liver and kidneys. These variability measurements were compared between our whole-body algorithm and a conventional bi-exponential fitting method.

Statistical analysis

Statistical analysis was performed using commercially available software (IBM SPSS Statistics, version 19, IBM Corp., Somers, NY, USA). For the evaluation of the inter-observer agreement, intra-class correlation coefficients (ICCs; absolute agreement, two-way mixed) were calculated. An ICC of 0.21 – 0.40 was considered to be indicative of fair agreement, 0.41 – 0.60 of moderate agreement, 0.61–0.80 of substantial agreement, and an ICC greater than 0.80 to be indicative of almost perfect agreement (ICC=1.00, perfect agreement) [19].

The coefficients of variation of D* and F_p were compared between our algorithm and the conventional fitting algorithm using paired Student t-tests with Bonferroni correction for multiple comparisons (yielding a *p*-value below 0.05/2= 0.025 to indicate statistically significant differences). The repeatability of D, D*, and F_P values (in all organs) was assessed in the three subjects who underwent a follow-up scan by calculating within-subject coefficients of variation.

Results

Acquisition time

Because of limited available scanner time, not all subjects were imaged from head to toe. Total scan times were 72 min (whole-body, n=4), 48 min (head to knee, n=2), and 36 min (head to proximal femur, n=2), respectively.

Parametrical maps

Exemplary coronal maps of D, D*, and F_p at different positions are shown in Figs. 1, 2, 3 and 4 (slice thickness 3.5 mm each). Structures of parenchymal organs could well be recognized on all three parametrical maps. The maps exhibited typical IVIM characteristics: CSF, renal pelvis, and bladder were all characterized by a high D value in the order of $2-3\times10^{-3}$ mm^2/s, consistent with unrestricted motion of the water molecules. On the other hand, D* and F_p were high in the renal pelvis compared to CSF, indicating faster flow of water molecules in urine being excreted compared to non-detectable flow of water molecules in the CSF. The liver was characterized by a lower D but higher F_p value compared to the renal cortex and medulla. Large vascular structures, such as the heart and the aorta, showed low D close to zero, but high D* and F_p values, consistent with predominantly fast moving water molecules.

Qualitative rating

The results of the qualitative rating and the inter-observer agreement are listed in Table 1. Depiction of anatomic structures was rated good on D maps and good (aorta) to fair (brain) on D* and F_p maps. Overall image noise was rated very little on D maps, little on D* maps and moderate on F_p

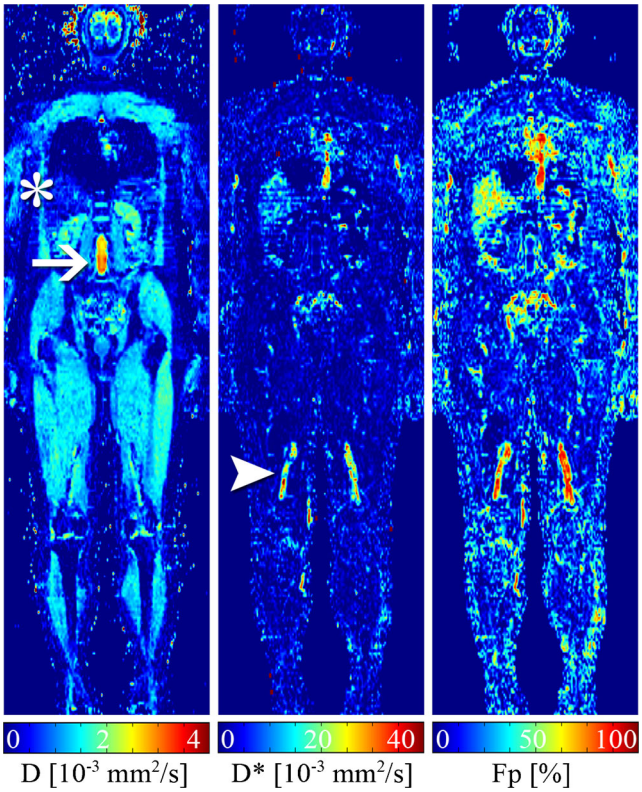

Fig. 1 Exemplary coronal whole-body maps of diffusion (D), pseudodiffusion (D*) and perfusion fraction (F_p) in a 31-year-old man. Slice thickness was 3.5 mm. The liver (*asterisk*) and the femoral vessels (*arrowhead*) are characterized by a low D but high D* and F_p values, indicating predominantly fast moving water molecules. On the contrary, the CSF (*arrow*) shows a high D but low D* and F_p values

maps. The inter-observer agreement was substantial to almost perfect (ICC=0.80 – 0.92).

Quantitative values and stability of IVIM algorithm

Typical signal intensities for different organs or body compartments and corresponding fitting curves are shown in Fig. 5. Without organ-specific adaptations, the algorithm provided stable IVIM parametric results for both parenchymal organs as well as fluid containing compartments. The percentage of voxels in which a monoexponential fit was applied (because F_P was<0 or>1) was highest in the renal medulla (13±7 %) and lowest in the cerebral white matter (5±3 %).

The mean values and standard deviations of the IVIM parameters are summarized in Table 2 and Fig. 6. The smallest D values were found for cerebral WM, whereas the highest D values were measured in the CSF. D* and F_p values were highest in the liver.

The coefficients of variation of D* and F_p were found to be significantly lower with the proposed whole-body algorithm compared to that obtained with a conventional algorithm in both the liver (D*: 2.46±0.81 vs. 4.91±1.26, $p<0.001$; F_p: 5.31±1.45 vs. 9.42±2.22, $p<0.001$) and the kidneys (D*: 2.28±0.88 vs. 4.59±1.07, $p<0.001$; F_p: 6.01±1.66 vs. 10.39±1.93, $p<0.001$), indicating significantly lower variability and thus higher stability of the whole-body algorithm.

Repeatability

Within-subject coefficients of variation and corresponding 95 % confidence intervals were: D, 8.4 % (4.1-12.6 %); D*, 18.2 % (14.0-22.5 %); F_p, 20.2 % (16.0-24.4 %).

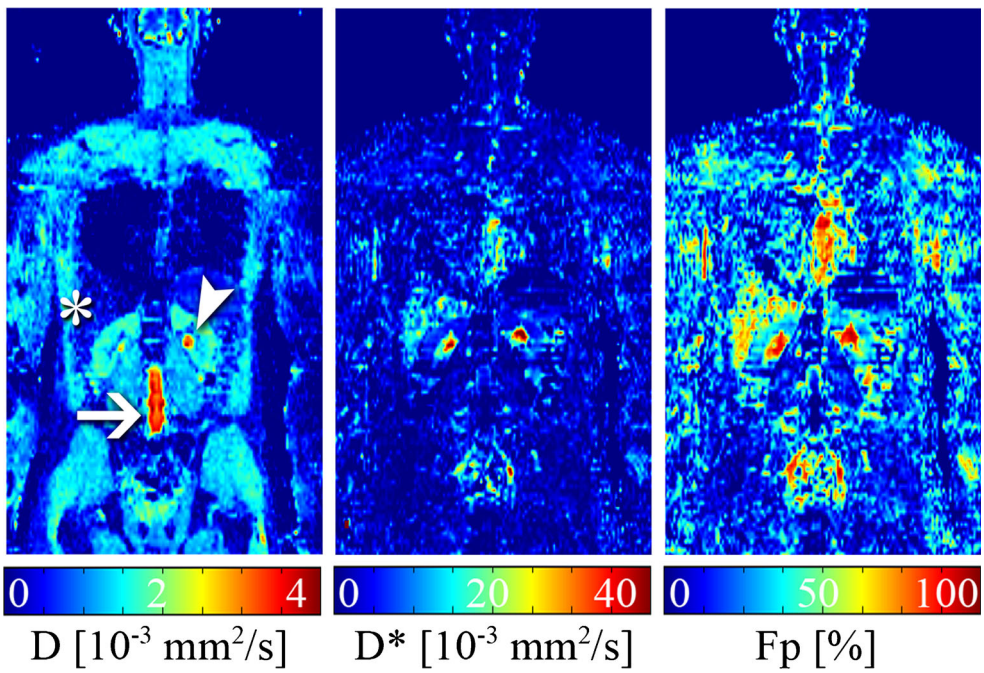

Fig. 2 Exemplary coronal maps of diffusion (D), pseudodiffusion (D*) and perfusion fraction (F_p) in a 27-year-old man. Slice thickness was 3.5 mm. Whereas D is high in both CSF (*arrow*) and renal pelvis (*arrowhead*), D* and F_p are considerably higher in the renal pelvis, indicating higher flow of the urine relative to the CSF. The liver is characterized by a lower D (*asterisk*) but higher F_p compared to the renal cortex

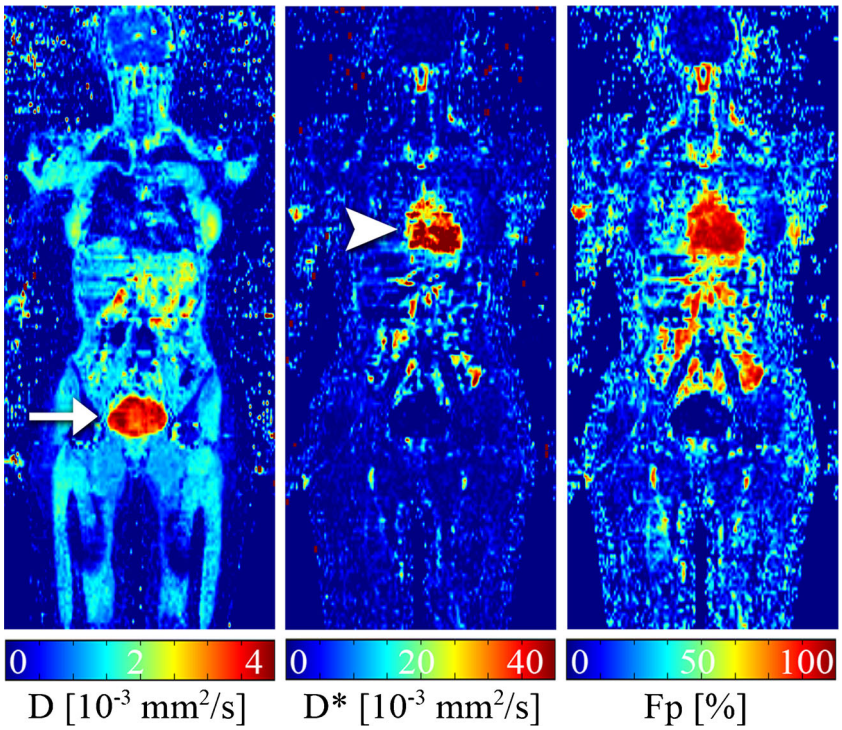

Fig. 3 Exemplary coronal maps of diffusion (D), pseudodiffusion (D*) and perfusion fraction (F_p) in a 34-year-old woman. Slice thickness was 3.5 mm. Whereas the heart (*arrowhead*) shows high D* and F_p values, D is low, indicating predominantly fast moving water molecules. By contrast, the bladder (*arrow*) is characterized by a high D but low D* and F_p values

Discussion

This study demonstrated the technical feasibility of whole-body IVIM imaging at 3 Tesla. The proposed approach allows consistent calculation of coronal whole-body parametrical maps of good to fair image quality.

Individual IVIM protocols have been applied for tissue characterization in specific organs [6–8, 12, 14, 15, 20–30].

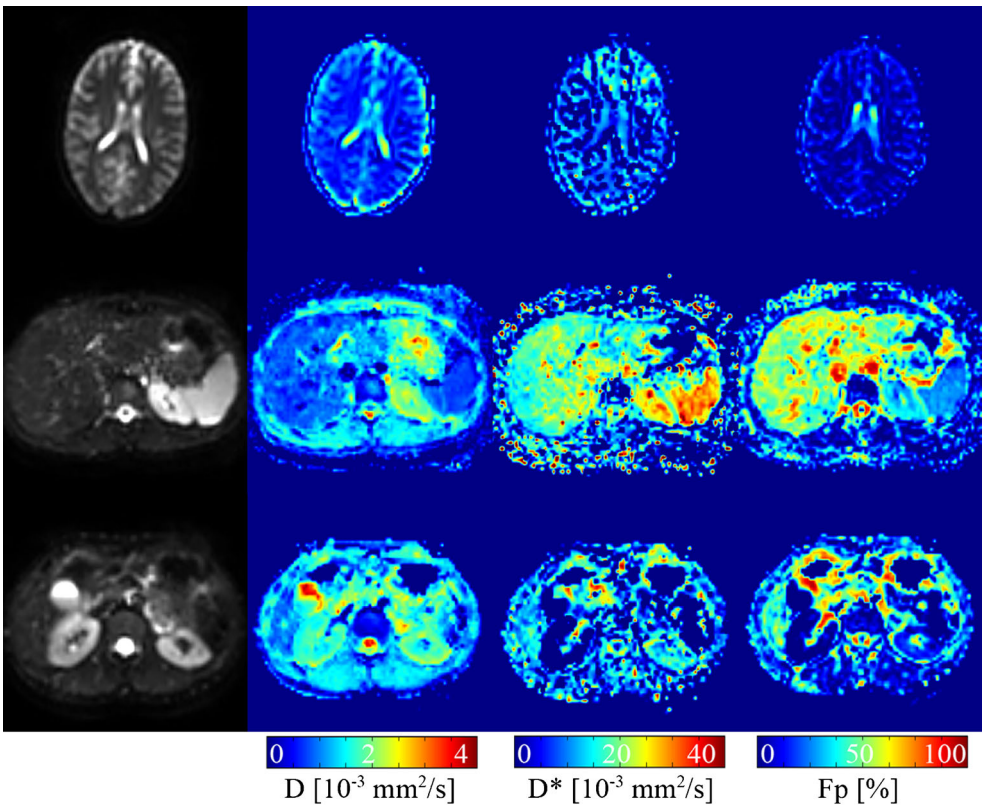

Fig. 4 Exemplary b0 images as well as maps of diffusion (D), pseudodiffusion (D*), and perfusion fraction (F_p) at the level of the brain, the liver, and the kidneys

Table 1 Qualitative rating of depiction of different anatomic structures and overall impression of image noise on coronal maps of diffusion (*D*), pseudodiffusion (*D**), and perfusion fraction (F_p) derived of all patients. All values are presented as median [inter-quartile range]. * 1 (excellent depiction), 2 (good depiction), 3 (fair depiction), 4 (poor depiction). ** 1 (very little), 2 (little noise), 3 (moderate noise), 4 (severe noise). *R1*, reader one; *R2*, reader two; *ICC*, intra-class correlation coefficient

	D (R1)	D (R2)	D* (R1)	D* (R2)	F_p (R1)	F_p (R2)	ICC
Brain*	2.0 [1.25-2.75]	2.0 [1.0-3.0]	3.0 [3.0-4.0]	3.5 [3.0-4.0]	3.5 [3.0-4.0]	3.5 [3.0-4.0]	0.91
Aorta*	2.0 [1.25-3.0]	2.0 [1.0-3.0]	2.0 [1.25-2.75]	2.0 [2.0-3.0]	2.0 [1.0-2.75]	2.0 [1.0-3.0]	0.92
Liver*	2.0 [1.25-3.0]	2.0 [1.0-2.75]	3.0 [2.0-3.0]	3.0 [2.0-3.75]	3.0 [2.25-3.75]	3.0 [2.25-3.0]	0.80
Kidney*	2.0 [2.0-3.0]	2.0 [1.25-2.75]	3.5 [2.25-4.0]	3.0 [2.25-4.0]	3.0 [2.0-4.0]	3.0 [2.0-3.75]	0.86
Overall image noise**	1.0 [1.0-2.0]	1.5 [1.0-1.75]	2.0 [2.0-3.0]	2.5 [2.0-3.0]	3.0 [2.0-3.75]	3.0 [2.0-3.0]	0.88

Our proposed whole-body IVIM algorithm differs from previously published approaches, as the requirement for a resilient algorithm for a variety of different tissues had to be addressed. It is an adaptation of an algorithm applied by Sigmund et al. [13] with the following modifications: (a) D is calculated from a linear least squares fit to the log-transformed high b-values, which is faster than the application of a mono-exponential fit. (b) If the calculation of the perfusion fraction F_p does not provide a percentage between 0 and 100 %, a mono-exponential fit to all b-values is applied to obtain more accurate D values and avoid meaningless values for F_p and D* for undetectable pseudodiffusion. (c) D* is not directly obtained from a bi-exponential fit, but from a linear least-squares fit to the low b-values and subsequent extraction of D* using the known perfusion fraction F_p and the diffusion coefficient D. This approach showed to provide a considerable increase of parameter stability with excellent description of the measurement points.

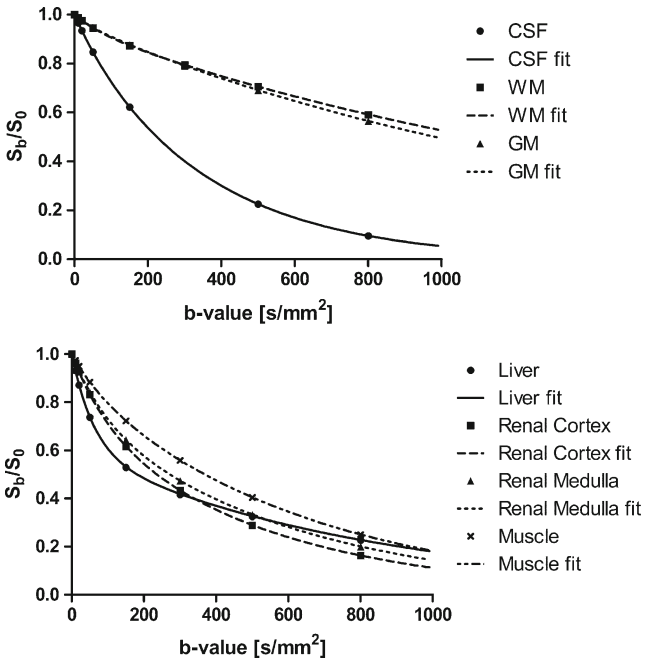

Fig. 5 Relative signal intensities at eight different b-values (0, 10, 20, 50, 150, 300, 500, and 800 mm^2/s) measured on axial slices obtained from one volunteer and corresponding fitted bi-exponential signal curves in different organs/compartments. The data-points are averaged over the entire region of interest for each organ. CSF, cerebrospinal fluid; WM, white matter; GM, grey matter

The obtained results are generally in line with former measurements in normal healthy tissue and compartments [6–10, 12–15, 17], with one important exception being the higher F_p and lower D* values in the liver. Potential explanations include the different IVIM algorithm and the lack of respiratory triggering in our protocol, which is not practical in a whole-body examination due to limited acquisition time. The free motion of the liver during image acquisition may have led to an overestimation of F_p due to breathing motion artefacts causing a subsequently lower D* in the following steps of the algorithm (the product of F_p D* was similar to that in previous studies [12]). The lack of compensation of breathing artefacts for parenchymal abdominal organs may be one disadvantage of the whole-body IVIM examination compared to dedicated organ-specific IVIM measurements. Moreover, free breathing may lead to pixel mismatch in abdominal investigations with impaired parameter value determination. Whereas DWI has proven feasible during free breathing with the phase shift not affecting image formation [31–33], this may not entirely apply for IVIM imaging.

The accuracy of D* and F_p calculation depends on the number of acquired b-values, especially those in the range of 0 – 50 [34]. Lemke et al. [35] suggested a minimum of 10 b-values for clinical applications, whereas in other studies the theoretical minimum of three b-values was used [36, 37]. In this whole-body study, images with eight different b-values were acquired to ensure acceptable accuracy and clinically viable acquisition times.

Currently, the main limitation of whole-body IVIM to clinical acceptance is its long scanning duration. Scan time can be improved by means of parallel imaging techniques such as GRAPPA or SENSE, as used in other IVIM studies [6, 12, 38]. We applied a relatively high SENSE factor of 3; further parallel imaging acceleration does not seem possible without image degradation. However, recent technical developments, such as simultaneous multi-slice acquisition which

Table 2 Mean values and standard deviations (*SD*) of diffusion (*D*), pseudodiffusion (*D**), and perfusion fraction (F_p) in different organs/compartments measured in the present whole-body study and reported values for healthy organs/compartments in organ-specific studies. *CI*, confidence interval

Year	Authors	Tesla	Number of b-values	Study Population	Organ/Compartment	D [x 10^{-3} mm^2/s], mean±SD	D* [x 10^{-3} mm^2/s], mean±SD	F_p [%], mean±SD	Respiratory triggering
2014	Filli et al. (present study)	3.0	8	N=8	CSF	2.91±0.16	10.02±4.37	3.77±2.88	No
					Cerebral white matter	0.64±0.05	14.27±3.64	3.25±0.94	
					Cerebral grey matter	0.67±0.05	12.33±4.06	3.48±1.56	
					Liver	0.91±0.23	17.48±6.75	47.07±14.40	
					Renal Cortex	1.74±0.16	15.57±6.48	20.92±4.39	
					Renal Medulla	1.64±0.21	16.18±5.33	23.55±8.27	
					Muscle (erector spinae)	1.58±0.06	16.32±1.72	10.22±3.05	
2013	Bisdas et al.	1.5	14	N=22	Cerebral white matter	0.62±0.21	7.3±6.1	6.5±3.7	
2013	Chiaradia et al.	1.5	10	N=15	Liver	1.23±0.45	49±32	29.08±15	Yes
2013	Dyvorne et al.	1.5	16	N=20	Liver				Yes/No
					- triggered, bipolar diffusion gradient (BP)	1.16±0.07	60.2±19.9	13.5±5.3	
					- triggered, monopolar (MP)	1.06±0.9	49.5±18.1	15.4±7.3	
					- free breathing, BP	1.20±0.06	68.3±26.9	13.3±4.8	
					- free breathing, MP	1.15±0.10	52.7±26.9	13.4±3.6	
2012	Andreou et al.	1.5	8	N=14	Liver	95 %CI 0.95-1.08	95 %CI 35.7-82.5	95 %CI 14.0-23.2	Yes
2010	Patel et al.	1.5	9	N=30	Liver	1.17±0.21	39.61±12.34	32.16±8.13	Partially
2012	Sigmund et al.	3.0	8	N=10	Renal Cortex	1.96±0.09	24.56±6.10	18.69±3.50	Breath-hold
					Renal Medulla	1.89±0.11	32.39±11.39	17.24±4.29	
2012	Ichikawa et al.	1.5	12	N=365	Renal Cortex	2.14±0.32	110±12.4	23.4±10.6	Yes
					Renal Medulla	2.10±0.34	40.7±9.82	29.7±9.34	
2012	Rheinheimer et al.	1.5	9	N=26	Kidney (parenchyma)	1.84±0.31	-	18.16±3.85	Breath-hold
2013	Sasaki et al.	1.5	11	N=24	Muscle (masticator muscles)	range 1.12-1.25	21.3±18.5 (masseter)	17±10 (masseter)	
2008	Qi et al.	1.5	24	N=13	Muscle (skeletal)	1.44±0.10	19.4±12.1	10.6±5.2	

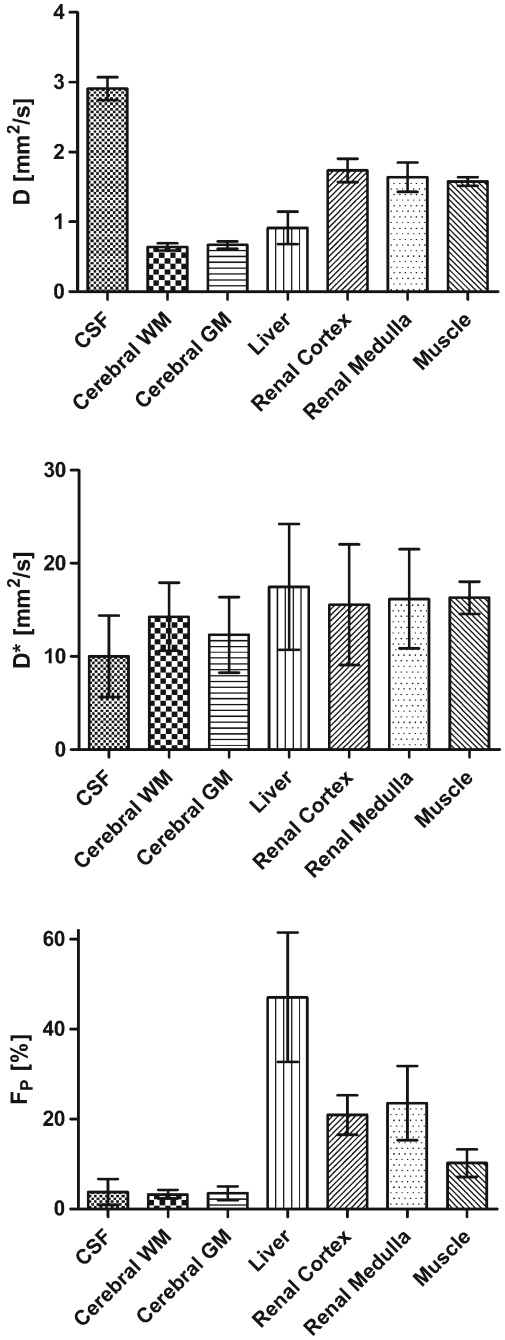

Fig. 6 Mean and standard deviation of diffusion (D), pseudodiffusion (D*) and perfusion fraction (F_p) measured in different organs/compartments. *CSF*, cerebrospinal fluid; *GM*, cerebral grey matter; *WM*, cerebral white matter

reduce the scan time by a factor of 2 – 4 [39, 40], raise confidence that the limitation of the long scanning duration may be overcome in the future. To further reduce scan time, acquisition of the lower limbs may be left out in most clinical settings, as usually performed in PET/CT imaging except for patients with melanoma [41, 42].

As compared to conventional whole-body DWI, a whole-body IVIM protocol provides a more comprehensive tissue characterization as it takes into account both diffusion and perfusion effects. IVIM may, therefore, be a complementary technique to whole-body DWI in the assessment of metastatic disease with tumour types exhibiting high tissue perfusion, such as neuroendocrine tumours, renal cell carcinoma, or melanoma. IVIM imaging is completely noninvasive and can be safely performed in case of concerns regarding the injection of contrast media, such as the risk of developing nephrogenic systemic fibrosis. Another potential application lies in the assessment of patients with widespread inflammatory myopathies, where whole-body MR imaging is a focus of current research [43]. Qi et al. found higher D and lower F_p values in inflamed muscle relative to normal muscular tissue [17]. However, it has to be investigated yet whether whole-body IVIM is able to depict focal lesions such as metastases accurately, as parenchymal organs show conceivable noise on the parametrical maps despite our improved algorithm.

In conclusion, whole-body IVIM imaging is feasible and allows the calculation of parametric IVIM maps of good to fair quality and repeatability. The proposed whole-body algorithm showed significantly higher stability compared to a conventional nonlinear square fitting algorithm. Applications of whole-body IVIM may include detection and characterization of widespread disease, such as metastatic tumours or inflammatory myopathies. The potential clinical value awaits further investigations.

Acknowledgements The scientific guarantor of this publication is Andreas Boss. The authors of this manuscript declare no relationships with any companies, whose products or services may be related to the subject matter of the article. The authors state that this work has not received any funding. No complex statistical methods were necessary for this paper. Institutional review board approval was obtained. Written informed consent was obtained from all subjects (patients) in this study. Methodology: prospective, experimental, performed at one institution.

References

1. Padhani AR, Liu G, Koh DM et al (2009) Diffusion-weighted magnetic resonance imaging as a cancer biomarker: consensus and recommendations. Neoplasia 11:102–125
2. Le Bihan D, Breton E, Lallemand D, Grenier P, Cabanis E, Laval-Jeantet M (1986) MR imaging of intravoxel incoherent motions: application to diffusion and perfusion in neurologic disorders. Radiology 161:401–407
3. Le Bihan D, Breton E, Lallemand D, Aubin ML, Vignaud J, Laval-Jeantet M (1988) Separation of diffusion and perfusion in intravoxel incoherent motion MR imaging. Radiology 168:497–505
4. Le Bihan D (1988) Intravoxel incoherent motion imaging using steady-state free precession. Magn Reson Med Off J Soc Magn Res Med / Soc Magn Reson Med 7:346–351
5. Turner R, Le Bihan D, Maier J, Vavrek R, Hedges LK, Pekar J (1990) Echo-planar imaging of intravoxel incoherent motion. Radiology 177:407–414

6. Chiaradia M, Baranes L, Van Nhieu JT et al (2013) Intravoxel incoherent motion (IVIM) MR imaging of colorectal liver metastases: are we only looking at tumor necrosis? J Magn Reso Imaging : JMRI. doi:10.1002/jmri.24172
7. Sasaki M, Sumi M, Van Cauteren M, Obara M, Nakamura T (2013) Intravoxel incoherent motion imaging of masticatory muscles: pilot study for the assessment of perfusion and diffusion during clenching. AJR Am J Roentgenol 201:1101–1107
8. Bisdas S, Koh TS, Roder C et al (2013) Intravoxel incoherent motion diffusion-weighted MR imaging of gliomas: feasibility of the method and initial results. Neuroradiology 55:1189–1196
9. Dyvorne HA, Galea N, Nevers T et al (2013) Diffusion-weighted imaging of the liver with multiple b values: effect of diffusion gradient polarity and breathing acquisition on image quality and intravoxel incoherent motion parameters–a pilot study. Radiology 266:920–929
10. Patel J, Sigmund EE, Rusinek H, Oei M, Babb JS, Taouli B (2010) Diagnosis of cirrhosis with intravoxel incoherent motion diffusion MRI and dynamic contrast-enhanced MRI alone and in combination: preliminary experience. J Magn Reso Imaging : JMRI 31:589–600
11. Yamada I, Aung W, Himeno Y, Nakagawa T, Shibuya H (1999) Diffusion coefficients in abdominal organs and hepatic lesions: evaluation with intravoxel incoherent motion echo-planar MR imaging. Radiology 210:617–623
12. Andreou A, Koh DM, Collins DJ et al (2013) Measurement reproducibility of perfusion fraction and pseudodiffusion coefficient derived by intravoxel incoherent motion diffusion-weighted MR imaging in normal liver and metastases. Eur Radiol 23:428–434
13. Sigmund EE, Vivier PH, Sui D et al (2012) Intravoxel incoherent motion and diffusion-tensor imaging in renal tissue under hydration and furosemide flow challenges. Radiology 263:758–769
14. Ichikawa S, Motosugi U, Ichikawa T, Sano K, Morisaka H, Araki T (2013) Intravoxel incoherent motion imaging of the kidney: alterations in diffusion and perfusion in patients with renal dysfunction. Magn Reson Imaging 31:414–417
15. Rheinheimer S, Stieltjes B, Schneider F et al (2012) Investigation of renal lesions by diffusion-weighted magnetic resonance imaging applying intravoxel incoherent motion-derived parameters–initial experience. Eur J Radiol 81:e310–e316
16. Morvan D (1995) In vivo measurement of diffusion and pseudodiffusion in skeletal muscle at rest and after exercise. Magn Reson Imaging 13:193–199
17. Qi J, Olsen NJ, Price RR, Winston JA, Park JH (2008) Diffusion-weighted imaging of inflammatory myopathies: polymyositis and dermatomyositis. J Magn Reso Imaging : JMRI 27:212–217
18. Gudbjartsson H, Patz S (1995) <Gudbjartsson_1995.pdf> Magn Reson Med Off J Soc Magn Res Med / Soc Magn Reson Med 34: 910–914
19. Kundel HL, Polansky M (2003) Measurement of observer agreement. Radiology 228:303–308
20. Yoon JH, Lee JM, Yu MH, Kiefer B, Han JK, Choi BI (2013) Evaluation of hepatic focal lesions using diffusion-weighted MR imaging: comparison of apparent diffusion coefficient and intravoxel incoherent motion-derived parameters. J Magn Reso Imaging : JMRI. doi:10.1002/jmri.24158
21. Ichikawa S, Motosugi U, Ichikawa T, Sano K, Morisaka H, Araki T (2013) Intravoxel incoherent motion imaging of focal hepatic lesions. J Magn Reso Imaging : JMRI 37:1371–1376
22. Chow AM, Gao DS, Fan SJ et al (2012) Liver fibrosis: an intravoxel incoherent motion (IVIM) study. J Magn Reso Imaging : JMRI 36: 159–167
23. Guiu B, Petit JM, Capitan V et al (2012) Intravoxel incoherent motion diffusion-weighted imaging in nonalcoholic fatty liver disease: a 3.0-T MR study. Radiology 265:96–103
24. Klauss M, Lemke A, Grunberg K et al (2011) Intravoxel incoherent motion MRI for the differentiation between mass forming chronic pancreatitis and pancreatic carcinoma. Investig Radiol 46:57–63
25. Dopfert J, Lemke A, Weidner A, Schad LR (2011) Investigation of prostate cancer using diffusion-weighted intravoxel incoherent motion imaging. Magn Reson Imaging 29:1053–1058
26. Sigmund EE, Cho GY, Kim S et al (2011) Intravoxel incoherent motion imaging of tumor microenvironment in locally advanced breast cancer. Magn Reson Med Off J Soc Magn Res Med / Soc Magn Reson Med 65:1437–1447
27. Bokacheva L, Kaplan JB, Giri DD et al (2013) Intravoxel incoherent motion diffusion-weighted MRI at 3.0 T differentiates malignant breast lesions from benign lesions and breast parenchyma. J Magn Reson Imaging: JMRI. doi:10.1002/jmri.24462
28. Federau C, Meuli R, O'Brien K, Maeder P, Hagmann P (2013) Perfusion measurement in brain gliomas with intravoxel incoherent motion MRI. AJNR American journal of neuroradiology. doi:10.3174/ajnr.A3686
29. Federau C, O'Brien K, Meuli R, Hagmann P, Maeder P (2013) Measuring brain perfusion with intravoxel incoherent motion (IVIM): initial clinical experience. J Magn Reso Imaging : JMRI. doi:10.1002/jmri.24195
30. Kim HS, Suh CH, Kim N, Choi CG, Kim SJ (2013) Histogram analysis of intravoxel incoherent motion for differentiating recurrent tumor from treatment effect in patients with glioblastoma: initial clinical experience. AJNR Am J Neuroradiol. doi:10.3174/ajnr.A3719
31. Kwee TC, Takahara T, Ochiai R, Nievelstein RA, Luijten PR (2008) Diffusion-weighted whole-body imaging with background body signal suppression (DWIBS): features and potential applications in oncology. Eur Radiol 18:1937–1952
32. Bammer R (2003) Basic principles of diffusion-weighted imaging. Eur J Radiol 45:169–184
33. Takahara T, Imai Y, Yamashita T, Yasuda S, Nasu S, Van Cauteren M (2004) Diffusion weighted whole body imaging with background body signal suppression (DWIBS): technical improvement using free breathing, STIR and high resolution 3D display. Radiat Med 22:275–282
34. Cohen AD, Schieke MC, Hohenwalter MD, Schmainda KM (2014) The effect of low b-values on the intravoxel incoherent motion derived pseudodiffusion parameter in liver. Magn Reson Med Off J Soc Magn Res Med / Soc Magn Reson Med. doi:10.1002/mrm.25109
35. Lemke A, Stieltjes B, Schad LR, Laun FB (2011) Toward an optimal distribution of b values for intravoxel incoherent motion imaging. Magn Reson Imaging 29:766–776
36. Concia M, Sprinkart AM, Penner AH et al (2013) Diffusion-weighted magnetic resonance imaging of the pancreas: diagnostic benefit from an intravoxel incoherent motion model-based 3 b-value analysis. Investig Radiol. doi:10.1097/RLI.0b013e3182a71cc3
37. Penner AH, Sprinkart AM, Kukuk GM et al (2013) Intravoxel incoherent motion model-based liver lesion characterisation from three b-value diffusion-weighted MRI. Eur Radiol 23:2773–2783
38. Lemke A, Laun FB, Simon D, Stieltjes B, Schad LR (2010) An in vivo verification of the intravoxel incoherent motion effect in diffusion-weighted imaging of the abdomen. Magn Reson Med Off J Soc Magn Res Med / Soc Magn Reson Med 64:1580–1585
39. Kong XZ (2014) Association between in-scanner head motion with cerebral white matter microstructure: a multiband diffusion-weighted MRI study. PeerJ 2:e366
40. Chang HC, Guhaniyogi S, Chen NK (2014) Interleaved diffusion-weighted improved by adaptive partial-Fourier and multiband multiplexed sensitivity-encoding reconstruction. Magn Reson Med Off J Soc Magn Res Med / Soc Magn Reson Med. doi:10.1002/mrm.25318

41. Niederkohr RD, Rosenberg J, Shabo G, Quon A (2007) Clinical value of including the head and lower extremities in 18F-FDG PET/CT imaging for patients with malignant melanoma. Nucl Med Commun 28:688–695
42. Querellou S, Keromnes N, Abgral R et al (2010) Clinical and therapeutic impact of 18F-FDG PET/CT whole-body acquisition including lower limbs in patients with malignant melanoma. Nucl Med Commun 31:766–772
43. Malattia C, Damasio MB, Madeo A et al (2013) Whole-body MRI in the assessment of disease activity in juvenile dermatomyositis. Ann Rheum Dis. doi:10.1136/annrheumdis-2012-202915